Mastering Syntheses of Siliceous Hierarchical Porous Self-Standing Monoliths through the Integration of Sol-gel Process, Complex Fluids and Planetary Mixer

Antoine Vardon, Marie Anne Dourges, Eric Laurichesse, Véronique Schmitt, Ahmed Bentaleb, Frédéric Nallet, Isabelle Ly, Rénal Backov

Mastering Syntheses of Siliceous Hierarchical Porous Self-Standing Monoliths through the Integration of Sol-gel Process, Complex Fluids and Planetary Mixer

Antoine Vardon[1], Marie-Anne Dourges,[2] Éric Laurichesse,[1] Véronique Schmitt,[1,*]

Ahmed Bentaleb,[1] Frédéric Nallet,[1,*] Isabelle Ly[1] and Rénal Backov[1]

[1] Université de Bordeaux, CRPP-UMR CNRS 5031, 115 Avenue Albert Schweitzer, 33600 Pessac, France. veronique.schmitt@crpp.cnrs.fr; nallet.frederic@crpp.cnrs.fr

[2] Université de Bordeaux, CNRS, Bordeaux INP, ISM, UMR 5255, 351 cours de la Libération, F-33405 Talence, Cedex, France.

Abstract

Self-standing siliceous monoliths bearing hierarchical porosity have been synthesized while combining sol-gel process, complex fluids and planetary mixer. The mechanically well defined and *a priori* reproducible stirring procedure leads to a precise control over the final hierarchical porous characteristics of the materials: Both the macroscopic cell and interconnecting throat dimensions in the monoliths, *i.e.* macroporosity, can be tuned by choosing the rotation speed. The fabrication process also leads to well-defined macrocellular wall thicknesses that can be tuned in the range 30–90 nm by stirring control. Final high internal phase emulsion-based siliceous materials—Si(HIPE)—are offering around 80-90% of porosity, decreasing with stirring speed, and broadly mixing-invariant BET specific surface area about 860±60 $m^2.g^{-1}$ where the microporous surface area is rather constant at 480±20 $m^2.g^{-1}$, the BJH (mesoporous) area being more spread in the range 380±80 $m^2.g^{-1}$.

Introduction

Porous materials are more and more present in our everyday-life, always in close connection with the industry and associated applications span over heterogeneous catalysis, environmental remediation (active or passive), acoustic or thermal insulation, bone tissue regeneration, to name a few.[1] Considering their intrinsic porosity, they are classified through the IUPAC nomenclature *versus* their pore sizes distribution as microporous from few Å to 2 nm, mesoporous from 2 nm to 50 nm and macroporous above 50 nm.[2] Typically, the microporosity is expressed through the void interstices between the employed molecular synthons. The mesoporosity may emerge either from the synthon higher scale organization

or can be induced while employing template molecules as mesogen phases (lyotropic mesophases concentrated above the Critical Micellar Concentration, CMC).[3,4,5] Macroporosity is most of the time induced through the physical chemistry of a complex fluid, employed still as a mold, playing for instance either with emulsions[6], air-liquid foams,[7,8] biliquid foams[9] or spinodal decomposition.[10] What is very interesting to observe or notice is the discrepancy between the pore sizes and the molecular synthon organization. Most of the microporous materials are rather highly crystalline, addressing for instance the scope of zeolite materials.[11] At the mesoscopic length scale, we found materials being still crystalline as the Metal Organic Frameworks (MOF)[12,13] coordination compounds, even if a new trend relies on MOF glassy systems,[14,15] or amorphous silica-based supports.[16,17] Indeed, when considering microporous materials, the unit cell can be easily spread at higher length scale where X ray diffraction or Small Angle X ray Scattering (SAXS) are appearing as the characterization tool of choice. At the mesoscopic length scale, the structure is still effective and accessible through SAXS, but defects are more and more important. When the porosity length scale is increasing towards the macroscopic length scale, the native large scale tortuosity is disrupting the unit cell replication into the geometric space, leading to more entropic materials, where diffractometers are useless as characterization tools.[18] Aside, in order to assess efficient and synergistic mass transport and reactivity, the actual trend is rather to address materials (self-standing the better) bearing a hierarchical porosity while including the above-mentioned micro, meso- and macroscopic length scales of porosity. To reach these complex materials bearing intrinsic hierarchical porosity, the synthetic mode of choice is certainly the *Integrative Chemistry* synthetic path proposed in our group in 2006.[19] In this vein, it is possible to generate hierarchical inorganic skeleton bearing hierarchical porosities through combining emulsions, lyotropic mesophases and sol-gel chemistry while dealing with silica (SiO_2) where the molecular SiO_4 synthon tetrahedral repartition into the

geometric space is random (inducing both statistical microporosity and amorphous nature of the matrix), leading to the Si(HIPE) series[9], (HIPE being the acronym for High Internal Phase Emulsions). This procedure has been later on extended with latex adjunction either in acidic or alkaline conditions.[20] More recently, we have developed materials labeled “MUB”, acronym for “Materials of the University of Bordeaux” corresponding to the one pot syntheses of binary MO_xSiO_2 (HIPE) series, where M = Co,[21] W,[22] Nb,[23] Ti,[24] or Cu[25] and being dedicated toward heterogeneous catalysis whether in liquid or gaseous phases.

This manuscript belongs to this vein of ultimately synthesizing catalytic-dedicated supports while intending to master the emulsification process, targeting its up-scalability. Up to now, all these inorganic supports were synthesized through a starting emulsification process (direct oil-in-water concentrated emulsion) employing small lab-scale, human-driven mortar and pestle, as it is the case for synthesizing the home-made French mustard or mayonnaise. Indeed, this process is not extendable to larger scales and may lack of repeatability, as the applied stirring is strongly linked both with the mortar diameter (at a given angular speed, the linear speed in a circular mortar varies with the mortar radius or diameter) and the operator intrinsic strength. Here, we present a normalized Si(HIPE) synthetic path through the integration of sol-gel process, complex fluids and a planetary mixer, this device being actually introduced not only for reaching repeatability in the HIPE elaboration, but also because planetary mixers are commonly used in the industry, both on a pilot scale or in production. The natively self-standing materials obtained using our normalized and up-scalable procedure, characterized in terms of hierarchical porosity and structure, exhibit narrower, and tunable distributions of properties compared to manually-prepared similar materials.

Materials and methods

Materials. High-purity dodecane (≥99%, density 0.75g/mL), hydrochloric acid 37 wt% (HCl), tetraethylorthosilicate (≥99%, TEOS), Tetradecyltrimethylammonium bromide (TTAB) were supplied by Alfa Aesar while tetrahydrofuran (THF, ACS-reagent) was purchased from Sigma-Aldrich. All the chemicals were used as received without any further purification. Deionized water was obtained using a Milli-Q water purification system.

Syntheses. Room temperature HCl (37 wt %, 5 g) was first added into 16 g of a 35wt% TTAB aqueous solution (also at room temperature), leading to a pH close to 0.05 (far below the silica isoelectric point reached at pH around 2.1). The choice of such acidic pH is driven with the endeavor of providing the siliceous network a rather fractal character (and not a Euclidean one) in order to both accommodate the oil-droplet interface curvature and address a higher degree of microporosity/mesoporosity. Then 5 g of TEOS is added. The choice of 5 g of TEOS is indeed an optimization between the aim of generating monolith-type materials (where the precursors concentration should be high enough to mineralize all the oil/water interfaces) while avoiding the ethanol production that is known to destabilize emulsions. TTAB has been chosen because it provides giant micelles in presence of salt above the critical micellar concentration and because it is a cationic surfactant. Indeed, a cationic surfactant (CTAB) has been employed in acidic condition to generate MCM-41 molecular sieves[26]. Considering the chosen pH and the cationic character of the surfactant, it has been proven that the positively charged silica precursors and the ammonium head group of the surfactant molecules association is occurring through the release of bromide anions.[27] The solution was stirred for 5 min both to promote TEOS full hydrolysis and allow the partial evaporation of ethanol resulting from the TEOS hydrolysis. This partial evaporation represents about 6.5 wt% of the ethanol produced at full conversion. Then, 37 g (49.3 mL) of dodecane was incorporated by manual stirring during 30 seconds before being emulsified

by the planetary mixer at respectively 200, 500, 1000, 1500 and 2000 rpm during 5 minutes. The planetary mixer in use is a Planetary Centrifugal Mixer SK-300SII from Kakuhunter, and the speeds mentioned above refer to *revolution* speeds, noted hereafter Ω, of the device that control the centrifugal force. The *rotation* speed that controls mixing has been fixed to 40% of the revolution speed, i.e. “mixing mode”, as recommended by the equipment manufacturer. The native direct oil-in-water emulsions were then easily flow-transferred into several polypropylene canisters with no noticeable effect of the mixing speed. The sol-gel process and aging are then let to proceed during 1 week. The dispersed phase volume fraction of the emulsion can be estimated to 69.5% considering that all the TEOS hydrolyzes and produced ethanol evaporates. After extraction from their canisters, the solidified emulsions were washed for 12 hours though immersion in THF to wash out mainly the oily phase. After extraction from the THF washing bath, the wet materials were dried slowly in a desiccator for 1 month and then further in air for 1 week. We would like to emphasize that both the sol-gel process and the washing procedures occurred at room temperature (around 25°C). A thermal treatment was applied to both sinter the silica network and calcine the TTAB surfactant used as a mesoscopic templating and emulsion stabilizing agent. This surfactant removal corresponds to an additional 7.1 vol% of voids. The thermal treatment was performed in air, as follows: a first temperature increase (2°C/min heating rate) was applied to reach 180°C, where a 6 hours plateau was imposed, followed by a second temperature ramp (heating rate of 1°C/min) to reach 700°C where a second 6 hours plateau was imposed. Finally, the cooling temperature was uncontrolled and governed by the oven intrinsic inertia. Materials are labeled hereafter as Si(HIPE)2000, Si(HIPE)1500, Si(HIPE)1000, Si(HIPE)500, Si(HIPE)200 where the last digits correspond to the revolution speed applied during the planetary-mixer-induced-emulsification.

Characterizations.

Scanning Electron Microscopy (SEM). Samples were properly broken and fixed to aluminum holders using silver paint. The fractured surfaces were metalized with gold/palladium sputtering. SEM images were acquired with a Hitachi TM-1000 tabletop scanning electron microscope operating with a 15 kV accelerating voltage.

Transmission Electron Microscopy (TEM). The samples were ground to a powder in a mortar then dispersed in ethanol. A drop of the suspension was placed and dried on a TEM copper grid covered with carbon film. The TEM pictures were obtained with a Hitachi H7650 TEM operating at 80 kV.

Small-Angle X-ray Scattering (SAXS). X-ray diffraction experiments were done on a XEUSS 2.0 device (XENOCS, Grenoble, France) with a GeniX3D system (XENOCS micro-focus copper anode source coupled to a FOX3D single reflection mirror) delivering a monochromatic 8 keV beam (Cu Kα, λ = 1.5418 Å). The beam was further collimated by a set of 2 motorized, scatter-less (4-blade) slits. The powdered samples were put into thin glass capillaries (optical path *ca.* 1.5 mm), and exposed–depending on experimental configuration —for 2 to 3 h. Data were collected by a two-dimensional DECTRIS PILATUS-300k detector (Baden-Dättwill, Switzerland) placed at a sample-to-detector distance of 1639 mm (two-hour exposure), or 2468 mm (three-hour exposure), both calibrated with a silver behenate standard, giving access to a range of scattering wave vectors q with a significant overlap between 0.004 $Å^{-1}$ and 0.4 $Å^{-1}$. Note that the XEUSS 2.0 device offers a wholly evacuated flight path, from the downstream end of the mirror to a few centimeters before the detector, including the samples. The 1D diffractograms (intensity I vs q) were obtained by processing the detector images (487x1228 pixels) with FOXTROT software (collaboration between XENOCS and the SOLEIL synchrotron (Gif-sur-Yvette, France) SWING beamline team).

Specific surface area assessments. A Micromeritics 3Flex surface characterization analyzer (Micromeritics Instrument Corp, Norcross, GA) was used for all measurements. Prior to measurement, the samples were activated under secondary vacuum at 110°C for 12 h. Activation at 350 °C for 12 hours was also performed for comparison and led to similar results, indicating that the outgassing procedure was efficient for both temperatures. Nitrogen (N_2) adsorption isotherms measured at 77 K were collected and interpreted using a multi-point Brunauer-Emmett-Teller (BET) analysis[28] for surface area determination over the range 0.05–0.30 relative pressure (P/P_0) and with a N_2 cross-section of 0.162 nm^2. The mesoporous surface area was determined using the Barrett, Joyner and Halenda (BJH) method[29] while the microporous surface area was estimated by the difference between the BJH mesoporous surface area and the BET surface area, assuming that the macroporous surface area is negligible.

Mercury porosimetry. Intrusion/extrusion mercury measurements were performed using a Micromeritics Autopore IV apparatus to determine the scaffolds' macrocellular characteristics.

Results and discussion

At the macroscopic length scale we can first notice that the synthetic path in use allows reaching monolith-type materials (**Figure 1A**). The overall monolith geometries are imposed by the containing canisters in which final emulsions were introduced (hemolysis tubes here).

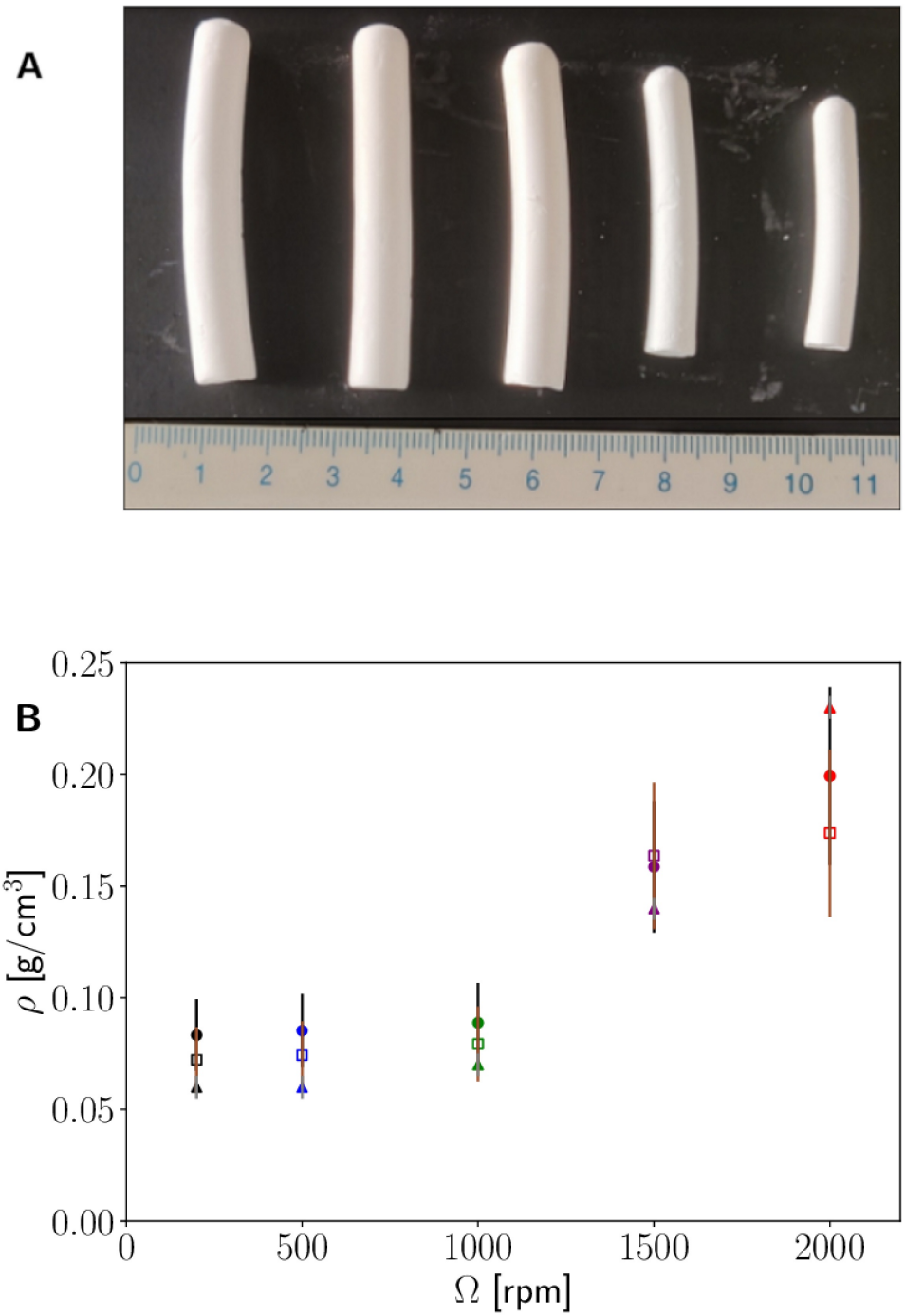

Figure 1. ***A)*** *Observation of the Si(HIPE) materials at the macroscopic length scale (tick spacing: 1mm) highlighting their monolithic character. From left to right: Si(HIPE)200, Si(HIPE)500, Si(HIPE)1000, Si(HIPE)1500, Si(HIPE)2000 and* ***B)*** *Density as a function of revolution speed with error bars. The solid triangles and gray bars are taken from Table 1 on mercury intrusion analyses further on; the solid circles and black bars represent values obtained from the mass to volume ratio where the volume is deduced from the measurement of the monolith dimensions using a Vernier caliper sampling the "diameter" at various heights and for various rotations along the "cylinder" axis, and mass is directly measured; the empty squares and sienna bars were obtained using volume estimates from image analysis*

Beyond the external shapes, it is obvious from **Fig. 1A)** that the monoliths dimensions (height and diameter, assimilating somehow irregular shapes to an ideal cylindrical shape) and therefore their volume vary as a function of the revolution speed used to produce the emulsions: The volume decreases for increasing revolution speed. The final volume can be estimated assuming a cylindrical geometry, and compared to the emulsion initial volume in the hemolysis tube (9.8 mL). This volume variation is expressed as an overall apparent density monotonously increasing with the revolution speed, see **Figure 1B)**, where it is displayed together with data from Hg porosimetry. Such a volume variation is commonly observed and depends on the initial drop size at constant oil volume fraction or, at fixed drop size, on oil volume fraction.[30] It is therefore a function of at least these two parameters. It has, of course, also been observed for monoliths obtained from emulsions produced with mortar-made-traditional Si(HIPE) while increasing the oil volume fraction[18]. In all cases the specific area $\bar{\Sigma}$ of the oil-water interface at the macro scale can tentatively be related to the drop size D_{macro} (that decreases for higher stirring[31]) and oil volume fraction ϕ: $\bar{\Sigma} = 6\phi / D_{macro}$, neglecting dispersity. Therefore, smaller drop sizes and/or higher volume fractions, the latter known to increase the elasticity and viscosity of the emulsion[32], also increase the specific area at the macroscopic scale. In both synthetic paths (traditional handmade and through the planetary mixer), the amount of TEOS, molecular precursor implied during the sol-gel process, is maintained constant to generate the Si(HIPE). A higher applied revolution speed leading to smaller drop sizes as shown below, the fabrication process should result in *i)* smaller void diameters since the oil droplets act as primary molds before monolith contraction (**Fig. 2A-E**) and to *ii)* higher interfacial area. From *ii)*, the silica shell thickness δ (or wall thickness) is expected to be thinner: Volume conservation indeed implies $\bar{\Sigma}\,\delta \equiv \phi_{SiO_2}$ being constant if all the TEOS condensates as SiO_2 at the macroscopic oil-

water interface, with therefore $\delta = \phi_{SiO_2} D_{macro} / (6\phi)$. We remind that the oil-water interface acts as defects where the silica heterogeneous nucleation is favored (minimizing the nucleation enthalpy) thereby favoring the oil/water interface mineralization. This is the reason why the monoliths' macroporosity resembles aggregated hollow spheres (**Figure 2A-E**). As the silica shell becomes thinner, stronger capillary forces apply during the gel drying, inducing a higher monolith shrinkage. This geometrical argument qualitatively explains the present correlation of volume reduction with revolution speed (**Fig. 1**), as well as the increased shrinkage observed with increasing oil volume fraction in the traditional Si(HIPE)[18].

It is worth noticing that for the higher stirring rate (2000 rpm), in addition to the image reported in **Fig. 2E** representing the majority of the sample, some domains made of silica spheres can be observed (**Fig. 2F**).

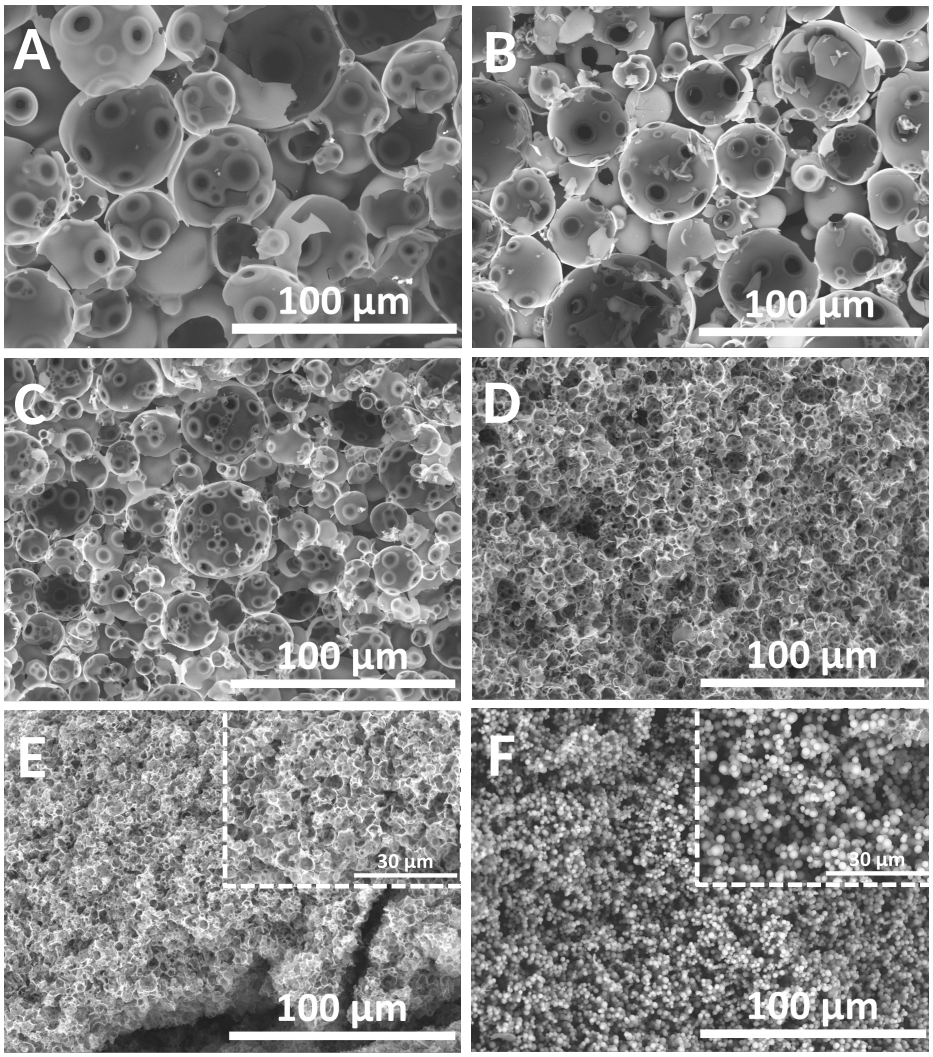

Figure 2*. SEM investigations at the macroscopic length scale. A) Si(HIPE)200, B) Si(HIPE)500, C) Si(HIPE)1000, D) Si(HIPE)1500, E) and F) Si(HIPE)2000.*

These silica spheres could be hollow or bulky (full spheres). To discriminate between these two possible morphologies higher resolution, Transmission Electron Microscopy (TEM) has been performed (**Figure 3**) after sample impregnation into a polymeric resin facilitating the cutting of a thin slice. From **Figure 3** highlighting very dark (high electronic contrast) objects, it can be concluded that the smaller spheres are indeed bulky.

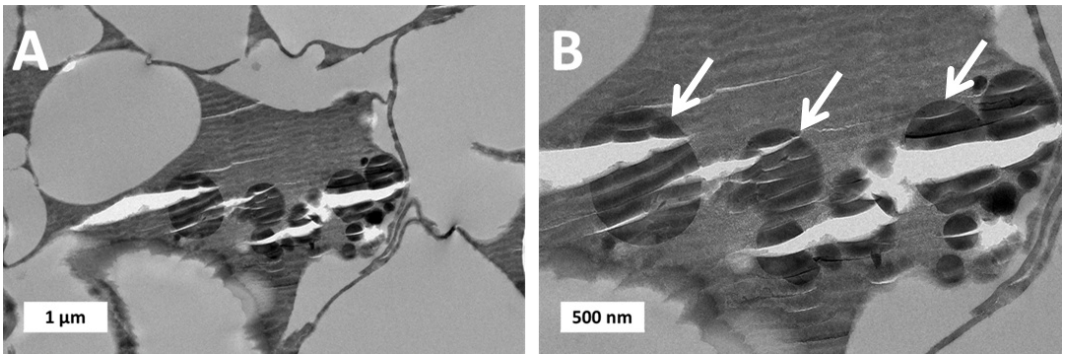

Figure 3*. A: Investigation of the small spheres in Si(HIPE)2000 at the mesoscopic length scale through TEM. B: Magnified version of the central part of A. The gray zones correspond to the previous voids filled by a resin while the dark zones highlighted by the white arrows (B) indicate full-silica spheres.*

We hypothesize that silica nucleation occurred in the emulsion continuous phase in addition to the heterogeneous nucleation at the macroscopic oil/water interface. This phenomenon has only been seen in the Si(HIPE)2000 sample and remains seldom, thereby not invalidating beforehand the assumptions leading to the scaling relationship $\delta = \phi_{SiO_2} D_{macro} / (6\phi)$—see however Supplementary Information for a more detailed critical analysis of the scaling law. Still at the macroscopic length scale, and in order to offer more quantitative characterization than the observation by SEM, we have performed mercury porosimetry. The first important point to underline is the fact that these planetary-mixer-made Si(HIPE) can withstand mercury imbibition, revealing a sufficient mechanical strength. Secondly, the geometries that constrain the mercury imbibition (**Figure 4**), that is to say the pores that are measured correspond to open throats between adjacent cells and/or interstices between adjacent cells but not to the diameters D_{macro} of the cells themselves since they do not exhibit any resistance to mercury imbibition. These pores may either results from previous drop contacts where no mineralization could take place, or from coalescence events (fusion between two drops in contact) that are arrested owing to the increase in viscosity during mineralization process inhibiting shape relaxation. This phenomenon could

then be compared to the partial coalescence arising in emulsions comprising solid content as crystallizable oils.[33,34] Indeed coalescence is a proposed mechanism as emulsions without TEOS and HCl are quite unstable and phase separate within approximately 10 minutes with the apparition of a macroscopic oil layer at the top of the sample.

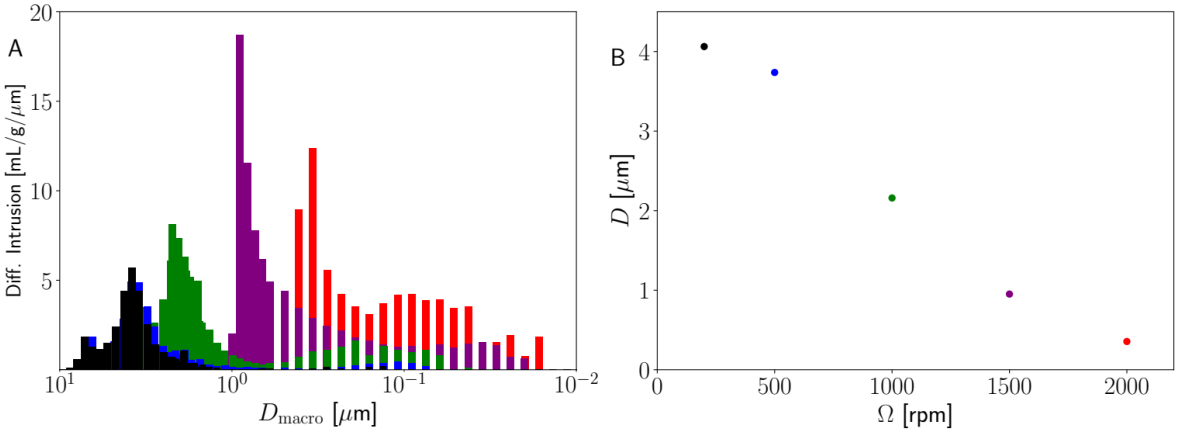

***Figure 4**. A) Pore size distribution obtained through mercury porosimetry. Si(HIPE)200 black, Si(HIPE)500 blue, Si(HIPE)1000 green, Si(HIPE)1500 lilac, Si(HIPE)2000 red. B) Derived maximal pore size as a function of the revolution speed.*

Overall, the pore sizes are decreasing with increasing the applied revolution speed. Also the pore size distributions spread towards smaller diameters with a more important population for the Si(HIPE)2000 monolith. A larger population is also seen on the pore size distribution by the occurrence of shoulder to the large size side of the main peak for 200 and 500 revolution speed. This could be a signature of the proposed arrested coalescence that is less prone for smaller drop sizes and higher viscosity that is to say higher stirring speeds.

Additionally, mercury porosimetry allows a measure of the porosity (macroporosity) expressed in vol%, as well as the bulk and skeleton densities (**Table 1**).

***Table 1**. Mercury porosimetry quantitative information. Bulk and skeletal densities as well as porosities (vol%).*

Sample	Bulk density ($g.cm^{-3}$)	Skeletal density ($g.cm^{-3}$)	Porosity (vol%)	Skeletal porosity (vol%)
Si(HIPE)200	0.06	0.87	93	60.5
Si(HIPE)500	0.06	1.24	95	43.6
Si(HIPE)1000	0.07	0.84	90	61.8
Si(HIPE)1500	0.14	1.18	88	46.4
Si(HIPE)2000	0.23	1.13	80	48.6

Note that the amorphous silica intrinsic density, ρ_{silica}, is equal to 2.2 $g.cm^{-3}$. The so-called skeletal density, noted hereafter $\rho_{skeletal}$, given in **Table 1**, is the density of the siliceous walls (mineralized matrix). As this value is always much below the silica density, this means that the walls themselves exhibit some porosity that can be deduced from the mismatch between the two densities (skeletal porosity=1- $\rho_{skeletal}/\rho_{silica}$). Such pores are actually mesopores, not accessible to mercury imbibition and that cannot be visualized on the pore size distributions of **Fig. 4A.** Their side effect on the $\delta(D_{macro})$ scaling law is further discussed in the Supplementary Information. The bulk density provided in **Table 1** is the apparent density of the monolith and is the result of the total porosity of the material (that is to say porosity coming from previous oil drops, surfactant calcination and wall mesoporosity). As already shown in **Fig. 1A**, it can be noticed that, starting with emulsions with identical composition, the total porosity decreased when the emulsification stirring speed increased. We think that this is a result of lower shrinkage and expected thinner silica shell for smaller drop sizes (higher interfacial area).

At the mesoscopic length scale, the mesoporosity has been first investigated through Transmission Electron Microscopy (TEM). Overall, the mesoscopic voids are rather poorly organized being essentially vermicular (**Figure 5**), despite the presence of some random domains being more organized into either a hexagonal packing (**Figure 5B, embedded**) or a cubic one (**Figure 5E, embedded**).

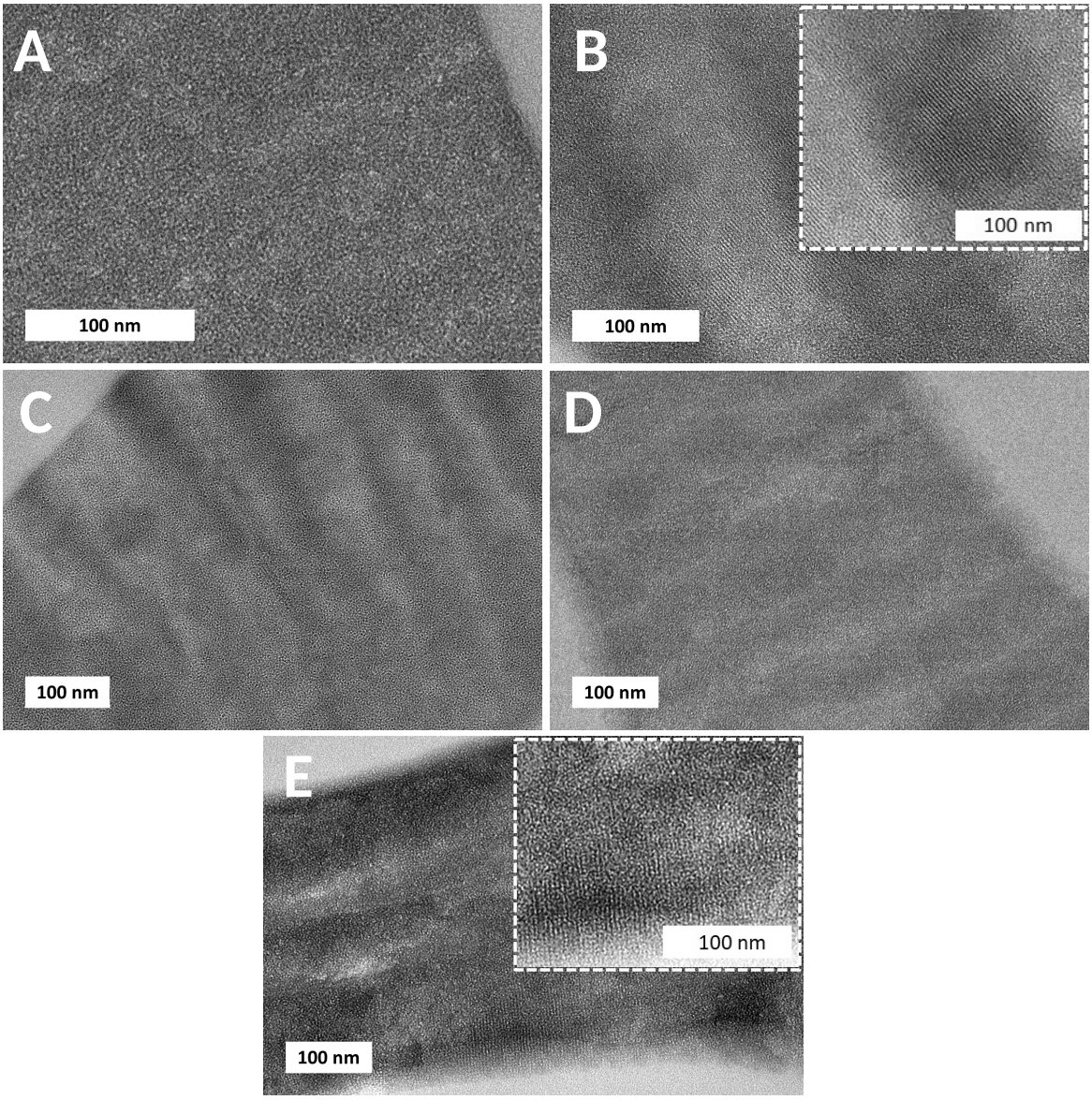

Figure 5*. Investigation at the mesoscopic length scale through TEM. A) Si(HIPE)200, B) Si(HIPE)500, C) Si(HIPE)1000, D) Si(HIPE)1500 and E) Si(HIPE)2000.*

TEM only provides discretized and local two-dimensional information. In order to assess further, with a better statistical significance the three-dimensional mesoscopic void organization in the bulk, Small Angle X-ray Scattering (SAXS) has been performed (**Figure 6**).

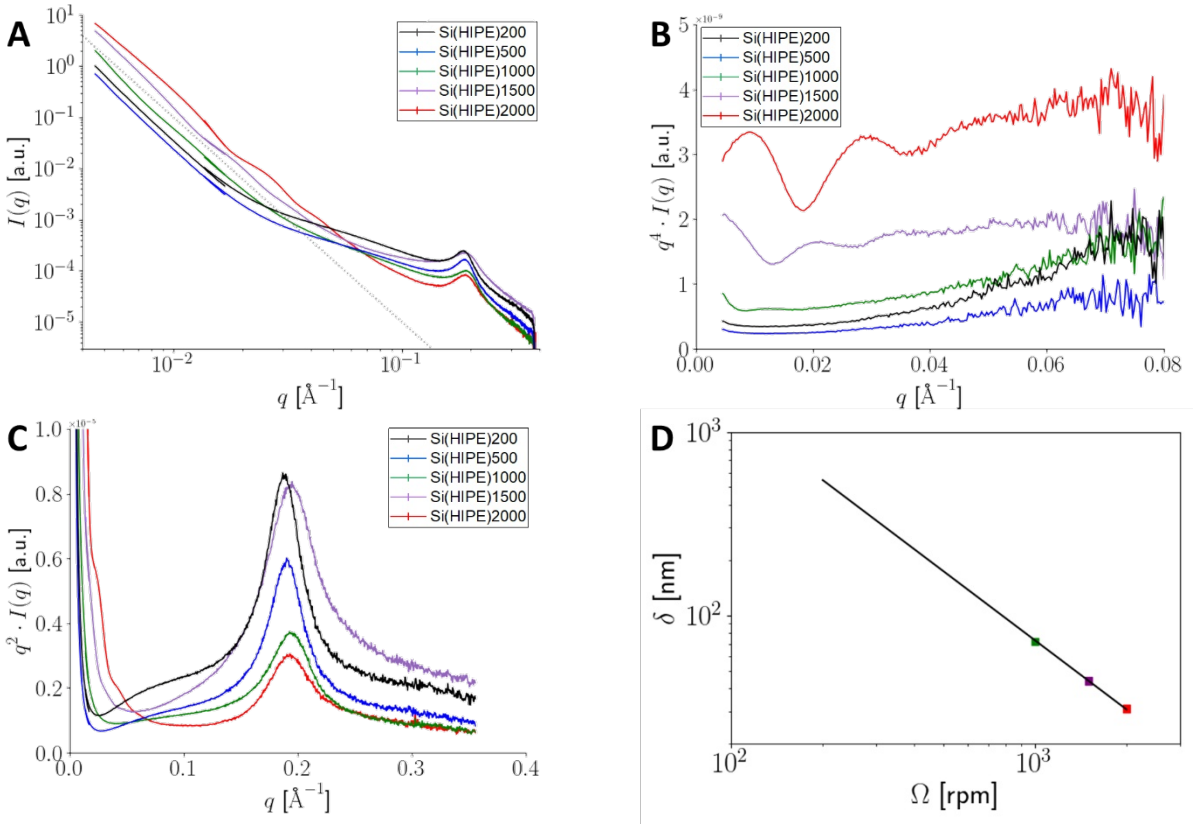

Figure 6*. Investigations at the mesoscopic length scale through SAXS. A) SAXS data – double logarithmic representation, emphasizing Porod's law (dotted gray line) B) SAXS data – Porod representation emphasizing form factor oscillations superimposed to the 1/q⁴ decay at small scattering wave vectors. C) SAXS data – Kratky representation, emphasizing local order. D) Measured (colored squares) and extrapolated silica shell thickness (solid black line:* $\propto \Omega^{-\nu}$ *with* $\nu \approx 1.2$*).*

The most obvious feature of the SAXS data is the power-law scattering intensity decrease with exponent -4 (**Figure 6A**), characteristic of locally plane, randomly oriented interfaces, also known as Porod's law.[35] Quite remarkable in the so-called Porod representation of the SAXS data—namely, $q^4 \cdot I$ *vs.* q (**Figure 6B**)—are the *small* wave vector intensity oscillations clearly observed for samples Si(HIPE)2000, 1500 and 1000. From sample Si(HIPE)2000 to Si(HIPE)1000, the leftmost peak oscillation is moving towards smaller values of the scattering wave vector q and eventually disappears, being shadowed by the beam stop of our SAXS set-up. It is difficult to tell whether the small intensity upturns noticed for samples Si(HIPE)500 and Si(HIPE)200 are actually the right

wing of a partly hidden oscillation, or rather come from unavoidable direct beam intensity tails originating in beam stop and collimating slit imperfections. The visible oscillations (samples Si(HIPE)2000, 1500 and 1000) come from the silica shells becoming thicker (and therefore detrimental as far as mass transport across the shells is concerned) with a decreasing emulsification speed. Indeed, with δ the distance separating the outer from the inner silica-air interfaces (silica wall thickness) assumed to be well-defined throughout irradiated Si(HIPE) samples of a given type, *interference terms* modify Porod's law[34], which becomes in this case: $I(q) \propto \sin^2(q\,\delta/2)/q^4$. Intensity peaks are therefore expected to be found at characteristic scattering wave vectors $q_k=(2k+1)\pi/\delta$, implying a constant interval $\Delta q=2\pi/\delta$ between consecutive peaks. From measured Δq (Si(HIPE)2000 and 1500), or guessed index k (k=2 for Si(HIPE)1000), the SAXS data is compatible with δ being close to 31, 44 and 72 nm for samples Si(HIPE)2000, 1500 and 1000, respectively (**Figure 6D** and Supplementary Information). The hexagonal or cubic structures, at *very small* spatial scales, appearing in **Figure 5**—with a stacking period of lines $d \sim 3$ nm in **Figure 5B** for instance—would lead (in the case of true long-range order) to first order Bragg peaks in the order of 0.2 $Å^{-1}$, close to the upper limit of the investigated q-range in our SAXS experiment. Such peaks, or peaked humps, are indeed clearly observed in the expected range (**Figure 6C**), and look very much the same for Si(HIPE) manually prepared with the traditional mortar and pestle method—see appropriate references to the MO_xSiO_2 (HIPE) series, where M = Co,[21] W,[22] Nb,[23] Ti,[24] or Cu[25] series. The location of the structural peak does not seem to be much affected by the revolution speed of the planetary mixer, staying in the range 0.189 – 0.195 $Å^{-1}$, with no obvious trend, as expected for a scale primarily determined by the TTAB surfactant self-assembly in water. In order to observe consistency for these SAXS-determined values, a SEM study was carried out to estimate wall thicknesses δ in the cases of Si(HIPE)2000, Si(HIPE)1500 and Si(HIPE)1000 (**Figure 7**). **Figures 7A** and **7B** depict

the structure of the Si(HIPE)2000 and Si(HIPE)1000 materials, respectively. From such pictures, the silica shells' thicknesses, δ can be extracted by image analysis. Such measurements performed for the Si(HIPE)2000, Si(HIPE)1500 and Si(HIPE)1000 samples (**Figures 7C, 7D and 7E**) evidence an increase of the silica shell thickness δ and a broadening of the size distribution while decreasing stirring speed, in agreement with SAXS investigations **(Figure 6B**). Aside, the respective average thicknesses are correlated with the macrocellular diameters average (**Figure 7F** and Supplementary Information, for a more in-depth discussion). We have already observed such a correlation between the siliceous thicknesses and the macroscopic cell diameters through a homothetic relation while dealing with dilute water-in-oil reverse emulsions generating silica capsules, the scaling law being interpreted in terms of mass conservation.[36] The average thicknesses can be compared with values obtained from SAXS measurements (**Figures 6B, 6D**) estimating thicknesses of 31, 44, 72 nm for Si(HIPE)2000, Si(HIPE)1500, Si(HIPE)1000 samples respectively, while from the SEM investigations, the estimated average thicknesses fall around 38 ± 4, 50 ± 5 and 92 ± 10 nm (with confidence interval of 95%) respectively. Overall, these measurements appear to be relatively close even if not identical.

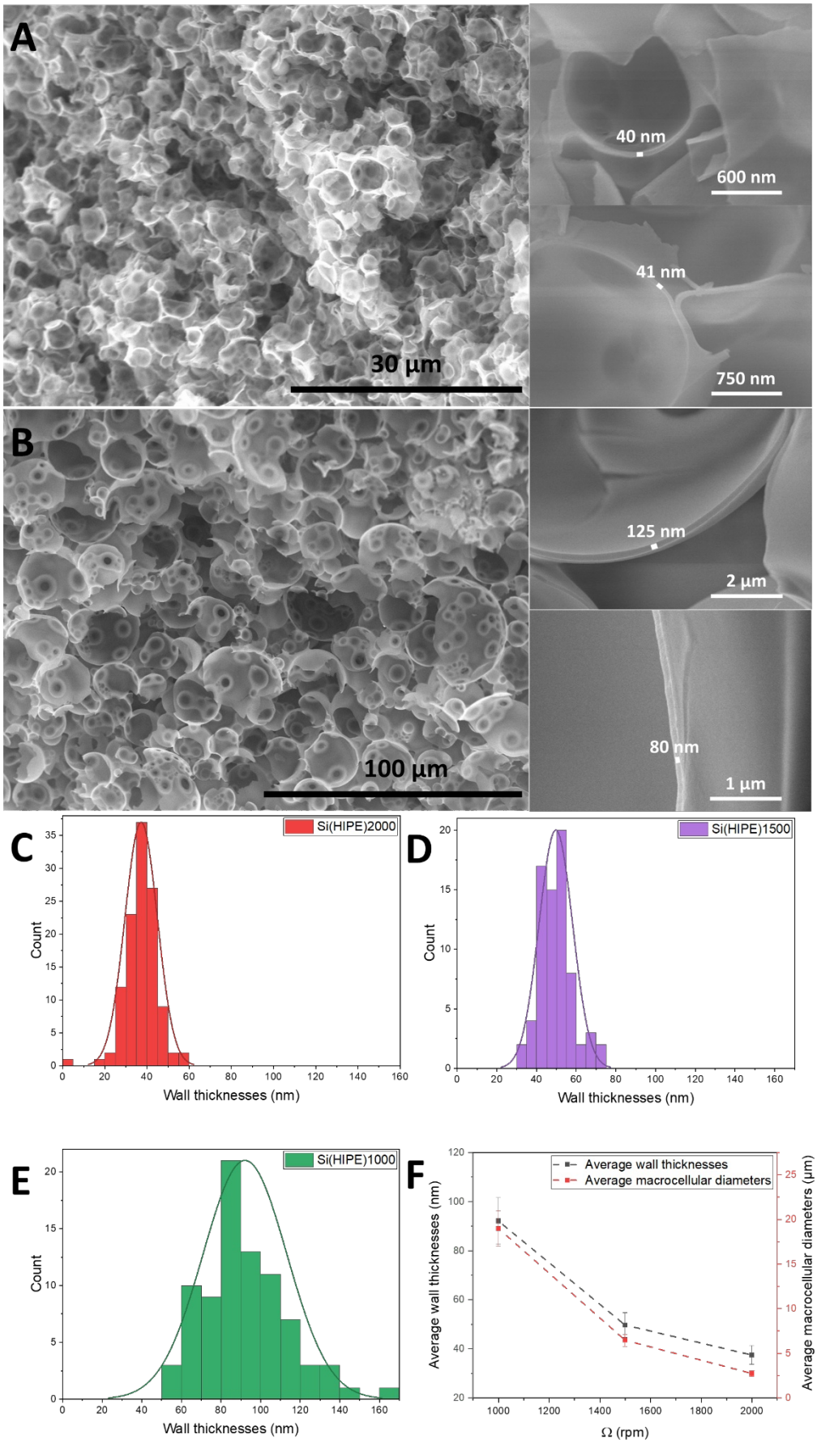
A
40 nm
600 nm
41 nm
750 nm
30 µm
B
125 nm
2 µm
80 nm
1 µm
100 µm
C
Si(HIPE)2000
Count
Wall thicknesses (nm)
D
Si(HIPE)1500
Count
Wall thicknesses (nm)
E
Si(HIPE)1000
Count
Wall thicknesses (nm)
F
Average wall thicknesses
Average macrocellular diameters
Average wall thicknesses (nm)
Average macrocellular diameters (µm)
Ω (rpm)

Figure 7*. SEM Investigations regarding the Plateau border thicknesses of the materials: A) Si(HIPE)2000, B) Si(HIPE)1000. Plateau borders' deconvolution using the ImageJ program for C) Si(HIPE)2000, D) Si(HIPE)1500, and E) Si(HIPE)1000. F) Evolution of silica wall thicknesses (black) and average macrocellular diameters (red) versus associated rpm. The dotted lines are for visualization purposes.*

For a further characterization of the meso- and microscopic length scales, nitrogen physisorption measurements have been performed (**Figure 8**).

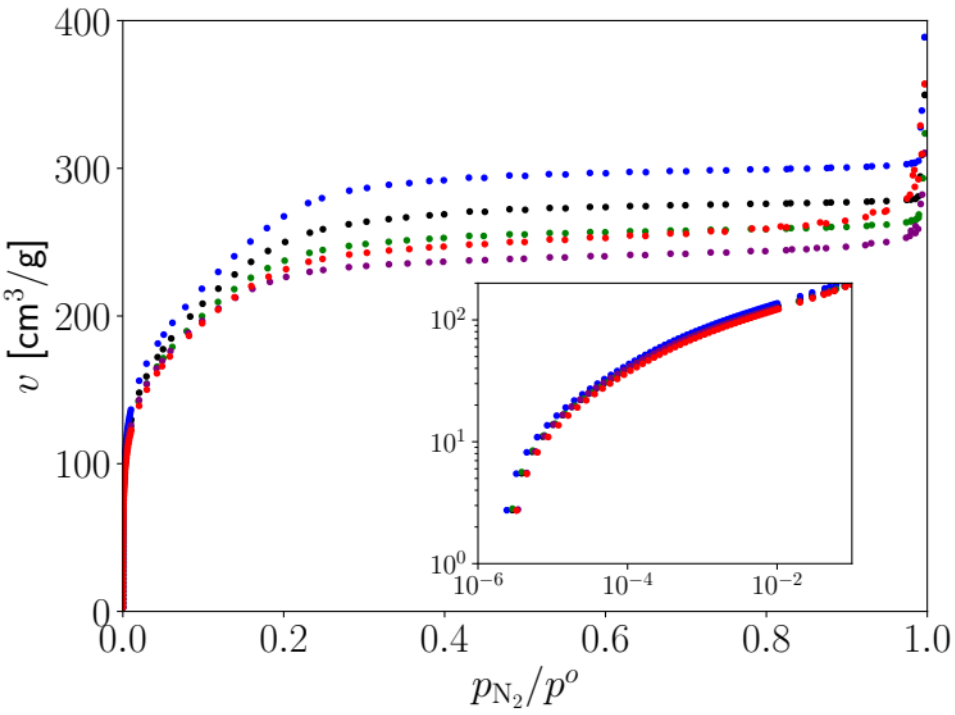

Figure 8*. Nitrogen physisorption measurements. Si(HIPE)200 black, Si(HIPE)500 blue, Si(HIPE)100 green, Si(HIPE) 1500 lilac, Si(HIPE2000) red. Inset in double logarithmic scales, emphasizing the initial, low relative pressure regime*

Hysteresis being negligible, both adsorption and desorption data appear plotted as super-imposed data. All isotherms are characteristic of a strong nitrogen adsorption at low relative pressure (up to *ca.* 10^{-2}), indicating microporosity (Type I isotherms),[2] followed with an extended plateau at medium relative pressure (0.2 – 0.9) and a final uptake at high relative pressure where a weak hysteresis loop can be observed solely for the Si(HIPE)2000 and Si(HIPE)1500 materials (mixed Type I and H3 isotherms),[2] indicating both

microporosity and a very wide distribution of pore sizes at the mesoscopic length scale. The strong up-take a high relative pressure (close to 1.0) is announcing the macroporosity for all materials.[2] Both BET and BJH surface areas have been estimated (**Table 2**).

***Table 2**. Surface areas determined using N_2 physisorption measurements. The BJH surface area are calculated from the adsorption curve.*

Sample	N_2-BET (m^2 g^{-1})	S_{micro} (m^2 g^{-1})	$S_{meso\ (BJH)}$ (m^2 g^{-1})
Si(HIPE)200	890	475	415
Si(HIPE)500	970	465	505
Si(HIPE)1000	840	480	360
Si(HIPE)1500	780	510	270
Si(HIPE)2000	815	455	360
Average	860	480	380
Standard deviation	74	21	86

When considering **Table 2**, the BET surface areas range from 780 m^2/g to 970 m^2/g, with no obvious trend as a function of Ω, where the microporous surface area is rather constant at 480 m^2/g and the BJH area (addressing the mesoporosity) being most often below the former, 380 m^2/g on average, with a significant dispersion. This feature is indeed the same as for the traditional Si(HIPE) materials obtained by hand, employing mortar and pestle as emulsifier tools[18].We have to underline that this micro-mesoscopic surface area is occurring within walls (δ) addressing thicknesses at the nanoscale (**Figure 7**). This feature is indeed very important, as it allows avoiding as far as it can be the limiting diffusion path/kinetic[16] when using as heterogeneous catalysts such materials, deploying a continuous nanoscale wall thicknesses up to the millimeter length scale. The nanoscale continuity, inducing the conspicuous self-standing character at the millimeter length and above (**Figure 1**), is vanishing the intrinsic flowability of powders depicting solely objects at the nanoscale. When considering **Figure 1**, it therefore appears that it is an advantageous feature to control the foams internal morphology, when dealing with catalytic supports, while maintaining a self-standing character, because the throats are the geometries limiting the convection that

drives the mass transport at the macroscopic length scale (Poiseuille flow).[37] Beyond mass transport, we have recently evidenced that the macroscopic morphology is also tuning the light transport into the foams, acting a “photonic sponges”[18,24].

CONCLUSION

We have presented here the first mechanized syntheses of Si(HIPE) matrices through the integration of sol-gel chemistry, direct concentrated emulsions, lyotropic mesophases and technology—namely a planetary mixer-based emulsification process. Even if mechanical emulsification is rather widely spread for usual emulsification, it remained a challenge for the preparation of Si(HIPE) owing to the fast kinetics of solidification making the samples difficult to handle. The macrocellular morphologies (wall thicknesses, cell diameters as well as the connecting throats diameters) can be varied through the applied revolution speed, with narrower distributions of properties with mechanical control than with manual control. We evidenced a scaling law between the cell diameters (in the range *ca.* 3–20 µm) and the wall thicknesses (ranging from *ca.* 30 nm to 90 nm), namely $\delta \propto D_{macro}^{1/2}$, involving in particular macroscopic surface area (oil droplet interfaces) to be mineralized with silicic acid ($Si(OH)_4$) generated as hydrophilic precursors, and area lost by connecting throats. These normalized Si(HIPE) materials exhibit around 80-90 vol% of porosity while addressing BET specific surface areas ranging from 800 $m^2\ g^{-1}$ to 970 $m^2\ g^{-1}$ where the microporous surface area is rather constant at 450-500 $m^2\ g^{-1}$ and the BJH (addressing the mesoporosity) being always lower and ranging from 270 $m^2.g^{-1}$ for the Si(HIPE)1500 up to 505 $m^2.g^{-1}$ for the Si(HIPE)500. This study is of first importance toward up-scaling the Si(HIPE) syntheses at the industrial level while offering both a straightforward and ease of reproducibility (operator independence), depicting a certain

process robustness, being still representative of the hand-made traditional Si(HIPE). We found out that the walls have well-defined, tunable thicknesses ranging at the nanoscale. At first, this nanoscale continuity, inducing a self-standing character at the millimeter length and above, inhibits the intrinsic flowability of powders made of solely discrete objects. Secondly, reduced nanoscopic thickness would limit less the diffusion path occurring at the mesoscale, optimizing thus mass transport as far as it can be within mesoscopic objects.

SUPPORTING INFORMATION:

Additional details relative to I) ethanol loss estimate, II) specific area related scaling laws (PDF) and III) Abbreviations and mathematical notations

ACKNOWLEDGMENTS:

Antoine VARDON acknowledges financial support by **RESCOLL – Société de Recherche** and **Conseil régional Nouvelle-Aquitaine** through Convention n° AAPR2021-2020-11931010. Authors also acknowledge Convention n° AAPR2021-2020-11931010 for subsidizing the acquisition of Hg-porosimetry and N_2-physisorption equipment. Authors declare no competing financial interest.

TOC Graphic

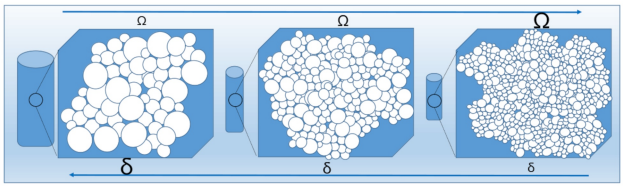

References

[1] Brun, N.; Ungureanu, S.;Deleuze, H.;Backov, R. Hybrid foams, colloids and beyond: From design to applications. *Chem. Soc. Rev*. **2011,** 40, 771-788

[2] Rouquerol, J.; Avnir, D.; Fairbridge, C. W.; Everett, D. H.; Haynes, J. M.; Pernicone, N.; Ramsay, J. D. F.; Sing, K. S. W.; Unger, K. K. Recommendations for the characterization of Porous solids. *Pure Appl. Chem.,* **1994**, 66, 1739-1758

[3] Schüth, F. Endo- and exotemplating to create high-surface-area inorganic materials. *Angew. Chem. Int. Ed.,* **2003**, 42, 3604-3622

[4] Feinle, A.; Elsaesser, M. S.; Hüsing, N. Sol–gel synthesis of monolithic materials with hierarchical porosity. *Chem. Soc. Rev.*, **2016**, 45, 3377-3399

[5] Roucher, A.; Emo, M.; Vibert, F.; Stébé, M-J.; Schmitt, V.; Jonas, F.; Backov, R.; Blin, J-L. Investigation of mixed ionic/nonionic building blocks for the dual templating of macro-mesoporous silica foams. *J. Colloid Interface Sci.,* **2019**, 533, 385-400

[6] Suzuki, K. ; Ikari, K. ; Imai, H. Synthesis of mesoporous silica foams with hierarchical trimodal pore structures. *J. Mater. Chem.* **2003**, 13, 1812-1816

[7] Gustafsson, H.; Holmberg, K. Emulsion-based synthesis of porous silica. A*dv. Colloid Interface Sci.,* **2017**, 247, 426-434

[8] Carn, F.; Achard, M.-F.; Babot, O.; Deleuze, H.; Reculusa, S.; Backov. R. Syntheses and characterization of highly mesoporous crystalline TiO_2 macrocellular foams. *J. Mat. Chem.,* **2005**, 15, 3887-3895

[9] Carn, F.; Colin, A.; Achard, M.-F.; Pirot, M.; Deleuze, H.; Backov, R. Inorganic monoliths hierarchically textured *via* concentrated direct emulsion and micellar templates. *J. Mat. Chem.* **2004**, 14, 1370-1376

[10] Kanamori, K.; Nakanishi, K.; Hanada, T. Spinodal decomposition in siloxane sol-gel systems in macroporous media. *Soft Matter*, **2009**, 5, 3106-3113

[11] Velty, A.; Corma, A. Advanced zeolite and ordered mesoporous silica-based catalysts for the conversion of CO_2 to chemicals and fuels. *Chem. Soc. Rev.*, **2023**, 52, 1773-1946

[12] Serre, C.; Millange, F.; Thouvenot, C.; Noguès, M.; Marsolier, G.; Louër, D.; Férey, G. Very Large Breathing Effect in the First Nanoporous Chromium(III)-Based Solids: MIL-53 or CrIII(OH). $\{O_2C{-}C_6H_4{-}CO_2\}\cdot\{HO_2C{-}C_6H_4{-}CO_2H\}_x\cdot H_2O_y$. *J. Am. Chem. Soc.*, **2002**, 45, 13519-13526

[13] Kapustin, E. A.; Lee, S.; Alshammari, A. S.; Yaghi, O. M. Molecular Retrofitting Adapts a Metal–Organic Framework to Extreme Pressure. *ACS Cent. Sci.*, 2017, **6**, 662-667

[14] Zhao, Y.; Lee, S.-Y.; Becknell, N.; Yaghi, O. M.; Austen Angell, C. Nanoporous Transparent MOF Glasses with Accessible Internal Surface. *J. Am. Chem. Soc.*, **2016**, 34, 10818-10821

[15] Bennett, T. D.; Coudert, F.-X.; James, S. L.; Cooper, A. I. The changing state of porous materials. *Nat. Mater.,* **2021**, 20, 1179–1187

[16] Roucher, A.; Blin, J.-L.; Schmitt, V.; Backov, R. Sol-gel process and complex fluids: sculpting porous matter at various lengths scales toward the Si(HIPE), Si(PHIPE) and SBA15-Si(HIPE) series. *J. Sol-Gel Sci. Technol*., **2019**, 90, 95–104

[17] Mahmoudi, Z.; Mesgari Abbasi, S.; Soleymani, F.; Khalaj, G.; Najafi, A. Development of sol-gel synthesis and characterization of meso porous SiO_2 nanopowder for improvement of nanomullite/SiC ceramic filter. *Ceram. Int.* **2025**, 51, 4918-4928

[18] Backov. R. Catalyseurs supportés modernes et efficaces obtenus par Chimie Intégrative. *Techniques de l'Ingénieur, Recherches et Innovations*, **2024**, J8300, 1-23

[19] Backov. R. Combining soft matter and soft chemistry: integrative chemistry towards designing novel and complex multiscale architectures. *Soft Matter*, **2006**, 2, 452-464

[20] Sen, T.; Tiddy, G.J.T.; Casci, J. L.; Anderson, M.W. . Meso-cellular silica foams, macro-cellular silica foams and mesoporous solids: a study of emulsion-mediated synthesis. *Microporous and Mesoporous Mater.*, **2005**, 78, 255–263

[21] Ly, I.; Vardon, A.; Chanut, N.; Nallet, F.; Pellenq, R. J.-M.; Rouzières, M.; Clérac, R.; Akil, J.; Epron, F.; Especel, C.; Backov, R. Binary CoO_x–SiO_2 Porous Nanostructures for Catalytic CO Oxidation. *ACS Appl. Nano Mater.*, **2022**, 5, 7331-7343

[22] Vardon, A.; Layan, E.; Louërat, F.; Nallet, F.; Bentaleb, A.; Dourges, M.-Anne; Toupance, T.; Laurichesse, E.; Sanchez, C.; Parizel, N.; Sidhoum, C.; Baaziz, W.; Ersen, O.; Pigot, T.; Backov. R. Hierarchical Porous WO_3@SiO_2 Self-Standing Monolithic Catalysts and Their Efficient Cycling "Cosolvent-Free" Friedel–Crafts Alkylation/Acylation Catalytic Properties. *Chem. Mater.*, **2023**, 16, 6502-6516

[23] Ly, I.; Layan, E.; Picheau, E.; Chanut, N.; Nallet, F.; Bentaleb, A.; Dourges, M.-A.; Pellenq, R. J.; Hillard, E. A.; Toupance, T.; Dole, F.; Louërat, F.; Backov, R. Design of Binary Nb_2O_5–SiO_2 Self-Standing Monoliths Bearing Hierarchical Porosity and Their Efficient Friedel–Crafts Alkylation/Acylation Catalytic Properties. *ACS Appl. Mater. Interfaces*, **2022**, 11, 13305-13316

[24] Layan, E.; Gupta, J.; Ly, I.; Nallet, F.; Bentaleb, A.; Laurichesse, E.; Vallée, R. A. L.; Blin, J.-L.; Lebeau, B.; Louërat, F.; Le Bechec, M.; Moonen, P.; Toupance, T.; Pigot, T.; Backov, R. TiO_2–SiO_2 Self-Standing Materials bearing Hierarchical Porosity: MUB-200(x) Series toward 3D-Efficient VOC Photoabatement Properties. *Langmuir*, **2023**, 11, 3871-3882

[25] Vardon, A.; Labarrère, H.; Nallet, F.; Chanut, N.; Weill, F.; Labrugère-Sarroste, C.; Bobet, J.-L.; Ly, I.; Epron, F.; Especel, C.; Backov, R. Designing CuO–SiO_2 and Cu0–SiO_2 Monolithic Ceramics Bearing Hierarchical Porosity Toward Robust and Cycling CO Oxidation Properties. *Chem. Mater.* **2023**, 1, 228-241

[26] Kresge, C. T.; Leonowicz, M. E.; Roth, W. J.; Vartuli, J. C.; Beck, J. S. Ordered mesoporous molecular sieves synthesized by a liquid-crystal template mechanism. *Nature*, 1992, **359**, 710–712

[27] Brinker, C. J.; Scherer, G. W. Sol-Gel Science *in "The Physics and Chemistry of Sol-Gel Processing", Academic Press*, **1990,** 1–912

[28] Brunauer, S.; Emmett, P. H.; Teller, E. Adsorption of Gases in Multimolecular Layers. *J. Am. Chem. Soc.* **1938**, 60, 309–319

[29] Barrett, E. P.; Joyner, L. G.; Halenda, P. P. The Determination of Pore Volume and Area Distributions in Porous Substances. I. Computations from Nitrogen Isotherms. *J. Am. Chem. Soc.* **1951**, 73, 373-380

[30] Destribats, M.; Faure, B.; Birot, M.; Babot, O.; Schmitt, V.; Backov, R. Tailored Silica Macrocellular Foams: Combining Limited Coalescence-Based Pickering Emulsion and Sol-Gel Process. *Adv. Funct. Mater.* **2012**, 22(12), 2642-2654

[31] Mason, T. G.; Bibette, J. Shear Rupturing of Droplets in Complex Fluids. *Langmuir* **1997**, 13, 4600-4613

[32] Mason, T. G. New fundamental concepts in emulsion rheology. *Curr. Opin. Colloid Interface Sci.* **1999**, 3, 231-238

[33] Boode, K.; Walstra, P. Partial Coalescence in Oil-in-Water Emulsions 1. Nature of the Aggregation. *Colloid Surface A* **1993**, 81, 121-137

[34] Thivilliers, F.; Laurichesse, E.; Saadaoui, H.; Calderon, F. L.; Schmitt, V. Thermally Induced Gelling of Oil-in-Water Emulsions Comprising Partially Crystallized Droplets: The Impact of Interfacial Crystals. *Langmuir* **2008,** 24(23), 13364-13375

[35] Porod, G. General Theory in *Small Angle X-ray Scattering*, O. Glatter, O. Kratky. Academic Press: New York **1982**, Chapter 2, 17−51

[36] Fornasieri, G.; Badaire, S.; Backov, R.; Mondain-Monval, O.; Zakri, C.; Poulin, P. Mesoporous and homothetic silica capsules in reverse-emulsion microreactors. *Adv. Mater*., **2004**, 16, 1094-1097

[37] Guyon, E.; Hulin, J. P.; Petit, L.; Mitescu, C. D. in *Physical Hydrodynamics*, Oxford University Press **2001** https://doi.org/10.1093/oso/9780198517467.001.0001

Supporting Information

Mastering Syntheses of Siliceous Hierarchical Porous Self-Standing Monoliths through the Integration of Sol-gel Process, Complex Fluids and Planetary Mixer

Antoine Vardon[1], Marie-Anne Dourges,[2] Éric Laurichesse,[1] Véronique Schmitt,[1,*] Ahmed Bentaleb,[1] Frédéric Nallet,[1,*] Isabelle Ly[1] and Rénal Backov[1]

[1] Université de Bordeaux, CRPP-UMR CNRS 5031, 115 Avenue Albert Schweitzer, 33600 Pessac, France. veronique.schmitt@crpp.cnrs.fr; nallet.frederic@crpp.cnrs.fr

[2] Université de Bordeaux, CNRS, Bordeaux INP, ISM, UMR 5255, 351 cours de la Libération, F-33405 Talence, Cedex, France.

Table of contents

Ethanol loss estimates

By simply weighing samples at the beginning and at the end, 5 min later, of the first step in the fabrication procedure (TEOS addition to the acidic TTAB micellar solution), we estimate the amount of evaporated ethanol to be 6.5wt%. In a linear approximation scheme (or zeroth-order kinetics), the characteristic evaporation time is estimated to be about 77min. With the standard assumption of a first-order evaporation kinetics, in about 6h 99wt% of the produced ethanol has been lost. While significant amounts of ethanol were still present when the gelifying oil-in-water emulsions were transferred into the polypropylene canisters, no ethanol remained 1 week later, at the end of the sol-gel and aging process.

Specific area scaling laws

In the **RESULTS AND DISCUSSION** section, the specific area $\bar{\Sigma}$ of the oil-water interface at the macro scale was related to the emulsion drop size D_{macro} and dispersed phase volume fraction ϕ by $\bar{\Sigma} = 6\phi / D_{macro}$ (neglecting size dispersity for simplicity), assuming area, respectively volume of a drop of size D_{macro} to be given by πD_{macro}^2, resp. $\frac{\pi D_{macro}^3}{6}$, that is to say assuming an *ideal* spherical shape. Since in the sol-gel process the amount of TEOS was kept constant, and if it can be assumed that all the produced silica covers the macroscopic oil-water interface, volume conservation implies $\bar{\Sigma}\delta \equiv \phi_{SiO_2}$, with ϕ_{SiO_2} being the SiO_2 volume fraction. Under such seemingly innocuous assumptions, a simple scaling law is expected, namely $\delta = \phi_{SiO_2} D_{macro} / (6\phi)$, where all quantities are either known from the fabrication process, or determined experimentally. The emulsion drop size distribution was obtained by image analysis of the available SEM data, and is reasonably well described by a log-normal size distribution, see **Figure S1**.

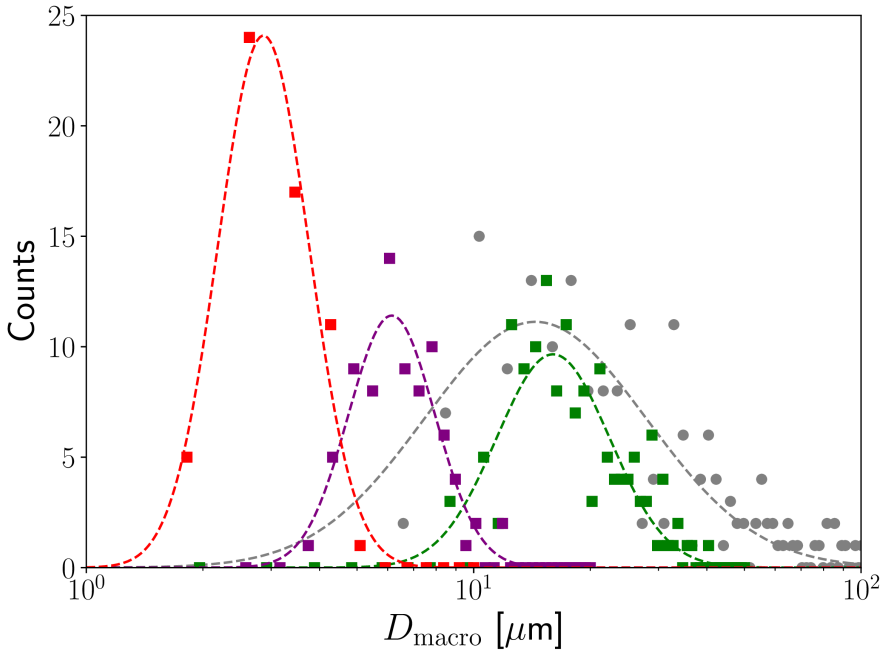

***Figure S1**: SEM investigations at the macroscopic length scale: Image analyses of data displayed in **Figures 2 and 7**, leading to drop size histograms. Mortar-and-pestle Si(HIPE) as gray dots, Si(HIPE)1000, 1500 and 2000 as green, lilac and red squares, respectively. A log-normal size distribution (dashed lines) has been fitted to data, with histogram peak and width as free parameters.*

The two relevant parameters, namely histogram peak D_{macro}^{peak} and width σ, are reported in the first rows of **Table S1**.

Table S1.

	Si(HIPE)	Si(HIPE)1000	Si(HIPE)1500	Si(HIPE)2000
D_{macro}^{peak} [µm]	22.3	18.0	6.6	3.1
σ [µm]	0.66	0.34	0.26	0.27
$D_{macro}^{peak} \times \Omega^{2.5}[a.u.]$	—	5.7	5.8	5.5
χ_{throat} [%]	—	55	33	22

From the width values σ, neglecting size dispersity seems a not too stringent approximation, and, from **Figures 2 and 7**, assuming an ideal spherical shape remains acceptable as far as *volume* estimates are concerned. Besides, while the mortar-and-pestle Si(HIPE) and Si(HIPE)1000 display, broadly speaking, about the same histogram peak, using the planetary mixer device clearly leads to a decrease in the size distribution width. In addition, as already observed when qualitatively commenting **Figure 2**, increasing the revolution speed Ω of the planetary mixer also significantly decreases the peak location D_{macro}^{peak}, which actually quite closely follows the scaling law $D_{macro}^{peak} \propto \Omega^{-2.5}$. Yet another scaling law has been observed at the mesoscopic length scale in SAXS, regarding the

variation of the silica wall thickness (**Figure 6B, 6D**), namely $\delta \propto \Omega^{-1.2}$. Assimilating D_{macro} to D_{macro}^{peak}, it therefore appears that the simple reasoning leading to $\delta = \phi_{SiO_2} D_{macro} / (6\phi)$ is *not* validated by our present measurements. Instead, SAXS and image analysis data are rather nicely described, as displayed in **Figure S2**, by the scaling law $\delta \propto D_{macro}^{1/2}$. Corrugations at the mesoscopic length scale of the SiO_2 walls, as observed directly in **Figure 5** (TEM) and, indirectly, in **Figure 6C** (SAXS), cannot explain this unexpected behavior because they would lead to an *excess* in specific area $\bar{\Sigma}$ compared to area predicted by the ideal spherical model, and therefore to *thinner* silica walls. The *missing area* associated to throats, that is to say to arrested coalescence events, observed in **Figure 2**, is thus presumably responsible for silica walls being thicker than naively expected. Quantitatively validating such an interpretation would require an experimental determination of the throat surface fraction χ_{throat} as a function of the revolution speed Ω, which has not been attempted. "Desirable" values for the throat surface fraction are nevertheless given in the last row of **Table S1**.

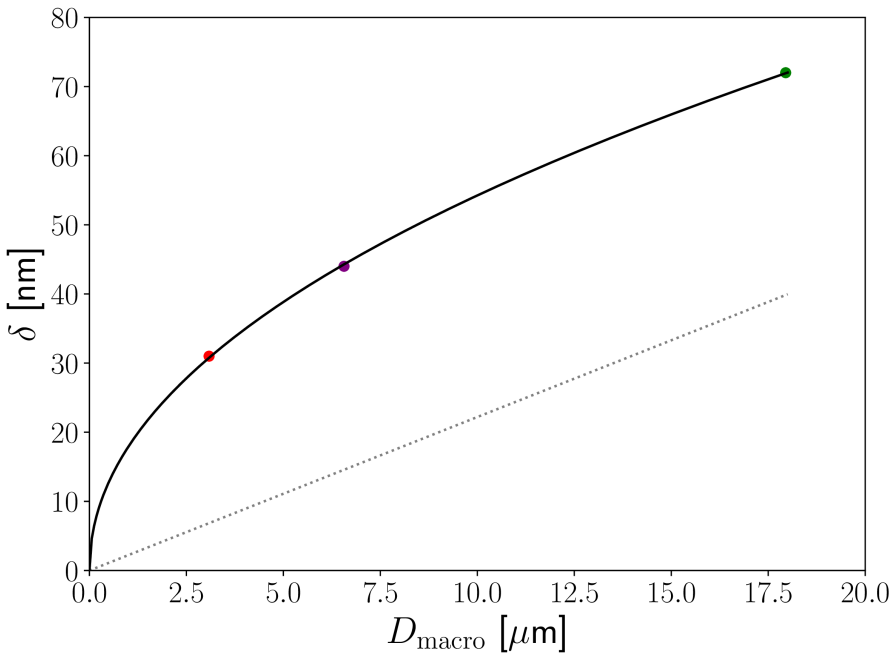

***Figure S2**: Wall thickness δ (SAXS data) as a function of the (peak) drop size D_{macro} for SI(HIPE)1000 (green), SI(HIPE)1500 (lilac) and SI(HIPE)2000 (red). Experimental scaling law $\delta \propto D_{macro}^{1/2}$: continuous black line. "Naive" scaling law $\delta = \phi_{SiO_2} D_{macro} / (6\phi)$ with $\phi_{SiO} = 8.7 \times 10^{-3}$ and $\varphi = 0.65$: dotted gray line*

Abbreviations and mathematical notations

Table S2

Description	Abbreviation, notation
Inorganic, silica-based material derived from high internal phase emulsions	Si(HIPE)
Brunauer, Emmet, Teller	BET
Barrett, Joyner, Halenda	BJH
International union of pure and applied chemistry	IUPAC
Critical micellar concentration	CMC
Metal-organic framework	MOF
Small-angle x-ray scattering	SAXS
Tetraethylorthosilicate	TEOS
Hydrochloric acid	HCl
Tetrahydrofuran	THF
Tetradecyltrimethylammonium bromide	TTAB
Revolution speed	Ω
Scanning electron microscopy	SEM
Transmission electron microscopy	TEM
X-ray wavelength	λ
Scattering wave vector	q
Scattered intensity	I
One-dimensional	1D
Mass density	ρ
Specific area	Σ
Drop size	D_{macro}
Oil volume fraction	ϕ
Shell thickness	δ
Silica volume fraction	ϕ_{SiO2}
Pore size	D
Silica intrinsic mass density	ρ_{silica}
Skeletal mass density	$\rho_{skeletal}$
Scaling law exponent	ν
Positive integer	k
Stacking period	d
Specific volume	v
Nitrogen pressure, standard pressure	P_{N2}, p^{O}
Throat surface fraction	χ
Surface areas	S_{micro}, S_{meso}
Log-normal distribution width	σ